Article

Consolidation of Zn-Hydroxyapatite and Zn-Bioactive Glass Composites Using High-Pressure Torsion

Amanda P. Carvalho [1], Andressa C. de O. Assunção [1], Jorgimara de O. Braga [2], Débora R. Lopes [1], Diogo M. M. dos Santos [1], Eduardo Henrique M. Nunes [1], Fernando Cotting [2] and Roberto B. Figueiredo [1,*]

[1] Department of Metallurgical and Materials Engineering, Universidade Federal de Minas Gerais, Belo Horizonte 31270-901, MG, Brazil

[2] Department of Chemical Engineering, Universidade Federal de Minas Gerais, Belo Horizonte 31270-901, MG, Brazil

* Correspondence: figueiredo@demet.ufmg.br

Abstract: There has been a great interest in developing zinc-based composites for biological applications. Mixing bioactive particles and obtaining a well-dispersed structure is not straight forward though. The present study reports a novel processing route in which zinc particles are mixed with hydroxyapatite and bioactive glass particles and consolidated at room temperature using high-pressure torsion. The composites display good dispersion of second phase particles, enhanced strength and an increased corrosion rate in the Hank's balanced salt solution. The incorporation of these particles can be used to tailor the corrosion rate of zinc. It is shown that the surface layer of the corrosion product in the zinc-bioactive particle composites is richer in calcium and phosphorous than the pure zinc counterpart.

Keywords: zinc matrix composites; biodegradable metals; high-pressure torsion

1. Introduction

Biodegradable metals have attracted significant attention in recent years due to their potential use as temporary implants [1]. Iron, magnesium and zinc are the most studied materials in this group due to their good biocompatibility and continuous well-known degradation in physiological media. However, their mechanical properties and corrosion behavior differ significantly. Changes in composition and the processing route have been investigated in order to attain better combinations of appropriate mechanical strength and corrosion resistance, without compromising biocompatibility.

Severe plastic deformation (SPD) techniques [2] have attracted attention as a potential processing route for many applications, including biodegradable metals. These techniques can refine the grain structure of metallic materials and produce ultrafine grained structures. Such grain refinement is usually linked to a pronounced increase in strength in these materials due to the well-known Hall–Petch effect [3–5]. Moreover, severe plastic deformation can improve corrosion resistance of metals and alloys [6,7]. Among the different SPD techniques, high-pressure torsion (HPT) [8] has emerged as a promising one. In this process, samples in the shape of discs or rings are pressed between rigid anvils and subjected to severe torsion straining through the relative rotation between these anvils. Thus, HPT has been widely used to process magnesium and its alloys [9] and a recent paper reviews the results focused on biological applications [10]. HPT has also been used to process iron and its alloys [11,12] and low corrosion rates in a Hank's solution have been reported for ultrafine grained iron [13]. Despite the significant improvement in properties, there are few studies on HPT processing of Zn-based materials [14–18] and most of these studies focus on mechanical properties.

In addition to the improvement in mechanical and corrosion properties, HPT has been used to consolidate particles to produce metal matrix composites (MMC). The high

compressive stresses and large shear straining enable the elongation of particles, breaking their surface oxide layer and promoting metallic bonding. Consequently, it is possible to incorporate different materials into a continuous metallic matrix. There has been a great interest in fabricating zinc matrix composites for biological applications by incorporating bioactive ceramic materials. For instance, zinc with beta-tricalcium phosphate [19,20] and hydroxyapatite (HA) [21,22] has been produced with spark plasma sintering. Zn-HA composites were also produced by hot extrusion of pressed particles [23]. There are now studies showing that Zn composites can be produced with HPT [16,24–27], but these studies were mostly focused on mixing metallic materials. Thus, the present study aimed to evaluate the effectiveness of HPT processing to consolidate Zn powders with bioactive particles. Both hydroxyapatite and bioactive glass are known to produce better interfacial bonds with hard tissues [28].

2. Materials and Methods

The materials used in the present investigation were pure Zn, hydroxyapatite (Sigma-Aldrich, St. Louis, MO, USA) and bioactive glass particles. The bioactive glass (BG) was prepared by sol-gel process and the precursors of the syntheses were tetraethyl orthosilicate (TEOS/98%, Sigma-Aldrich), triethyl phosphate (TEP, $\geq$99.8%, Sigma-Aldrich) and calcium nitrate tetrahydrate ($(Ca(NO_3)_2).4H_2O$, $\geq$99.8%, Vetec/Sigma-Aldrich). A detailed description of the synthesis and characterization of this BG is given in a previous study [29].

Preliminary tests were carried out to evaluate the minimum number of turns in HPT required for consolidation. Discs with 10 mm diameter and 1 mm thickness were produced by pressing pure Zn particles. These discs were processed by HPT using quasi-constrained equipment and a nominal pressure of 3.8 GPa. Samples were processed using 5, 10, 15 and 20 turns at room temperature. The effect of the number of turns on the consolidation was evaluated by observation of the structure and hardness distribution. Thus, Figure 1 shows the longitudinal section and hardness of the different samples. A continuous Zn matrix with isolated islands of ZnO was observed in all samples. The initial Zn particles contain a surface layer of ZnO, which is incorporated into the matrix during consolidation. Homogeneous hardness distribution, with an average value of ~50 Hv, was observed in all samples, except for the sample processed using 5 turns, which displayed a region with lower hardness near the center. This reduced hardness suggests a lack of consolidation in this region and therefore the composites were produced using 10 turns of HPT.

Pure Zn, Zn-10 wt.% HA and Zn-10 wt.% BG were mixed and pressed to ~100 MPa into discs with 10 mm diameter and 1 mm thickness. These discs were then processed with 10 turns of HPT at room temperature using a nominal pressure of 3.8 GPa. Quasi-constrained anvils were used for processing and the rotation rate was set to 1 rpm. This rotation rate is expected to generate negligible heating during processing [30]. The structure of the processed discs was observed using a JEOL 6360LV Scanning Electron Microscope (SEM) coupled with energy dispersive X-ray spectroscopy (SEM/EDX). The surface was ground and polished to a mirror-like finish before observation.

The microhardness distribution was evaluated along the disc surface. Thus, approximately 25 indentations were made along the diameter of the disc using Vickers indenter, a load of 100 gf and a dwell time of 10 s. The hardness was estimated as the average of each indentation. Dynamic hardness tests were used to estimate the strength and strain-rate sensitivity of each sample. Thus, a load of 300 mN was applied and maintained for 300 s while the variation in indentation depth was tracked using Shimadzu DUH-211s equipment. The data of indentation depth were plotted as a function of the time and the strain rate sensitivity was evaluated using a procedure suggested elsewhere [31].

Plane strain compression tests [32] were carried out at a strain rate of 10^{-3} s^{-1}. The discs' edges were ground to attain parallel surfaces with 7 mm width. The top and bottom were also ground to attain parallel surfaces with ~0.7 mm thickness. The plane strain compression device had a width of 1.4 mm. The tests were carried out using an Instron

equipment model 5582. Load and displacement data were converted to effective stress and effective strain considering plane strain conditions [32].
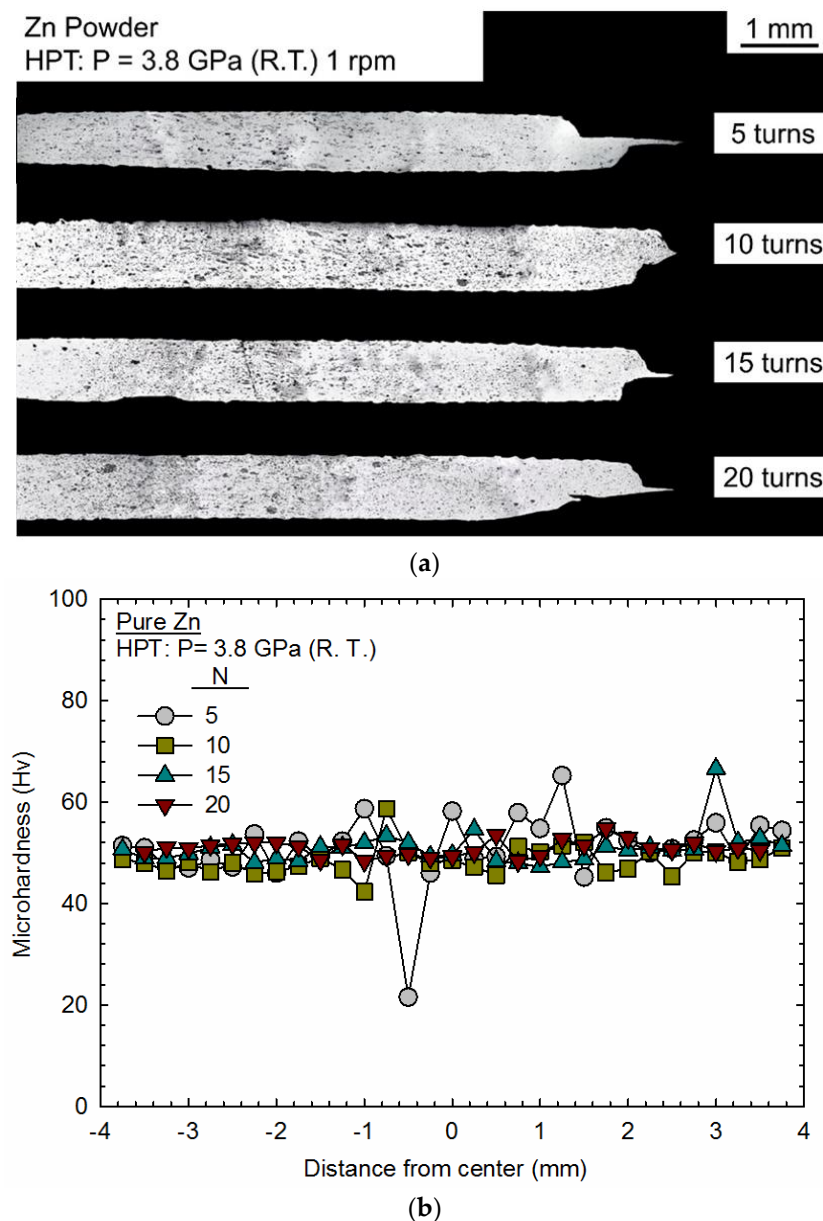

(a)

(b)

Figure 1. (**a**) Longitudinal sections and (**b**) hardness distribution in samples of pure Zn consolidated with HPT using a different number of turns.

The corrosion behavior was evaluated using electrochemical techniques in Hank's balanced salt solution (H1387, Sigma-Aldrich). The tests were conducted at room temperature using an electrochemical workstation (Gamry, Reference 600 Potentiostat). Three measurements were taken for each sample group. A three-electrode cell with $Ag/AgCl_{(KClsat)}$ as a reference electrode, platinum as the counter electrode and the composite as the working electrode was used. The open circuit potential (OCP) of each sample was monitored for 3600 s. The electrochemical impedance spectroscopy (EIS) measurement was performed by applying 5 mV (RMS) perturbation, in the frequency range of $0.01–10^5$ Hz, with 10 points for decade. The potentiodynamic polarization test was conducted at a scanning rate of 0.167 mV/s in a range of ±300 mV regarding OCP. The working electrode exposed

area in all electrochemical tests was 0.126 cm^2. The corrosion rate was calculated using Equation (1) [33,34]:

$$CR = 3.27 \times 10^{-3} \times \frac{i_{corr} EW}{\rho} \tag{1}$$

where i_{corr} is the corrosion current density ($\mu A/cm^2$) extracted from linear fit and Tafel extrapolation for the anodic curve for Zn-10% HA and cathodic curve for Zn and Zn-10% BG, EW is the corresponding equivalent weight and ρ is the density of corroding material (g/cm^3). Zinc, hydroxyapatite and bioglass density was 7.13 g/cm^3, 3.16 g/cm^3 [35] and 2.70 g/cm^3 [36], respectively. Some samples were immersed in Hank's solution for 24 h and the surface was then observed using SEM.

3. Results

3.1. Consolidation and Mechanical Properties

The surface of the discs of pure Zn, Zn-10% HA and Zn-10% BG consolidated with HPT is depicted in Figure 2. A continuous matrix and isolated islands of the second phase are observed in all samples. Details of the edge and center areas are also shown, revealing differences in the size of the reinforcement phase. The reinforcement phase particles appear larger in the center of the discs and smaller near the edges. This is attributed to the difference in shear strain imposed in these areas. The larger shear strain imposed on the edges of the discs can break these particles and promote better mixing with the metallic matrix. However, some cracks are visible near the edges of the Zn-BG composite.
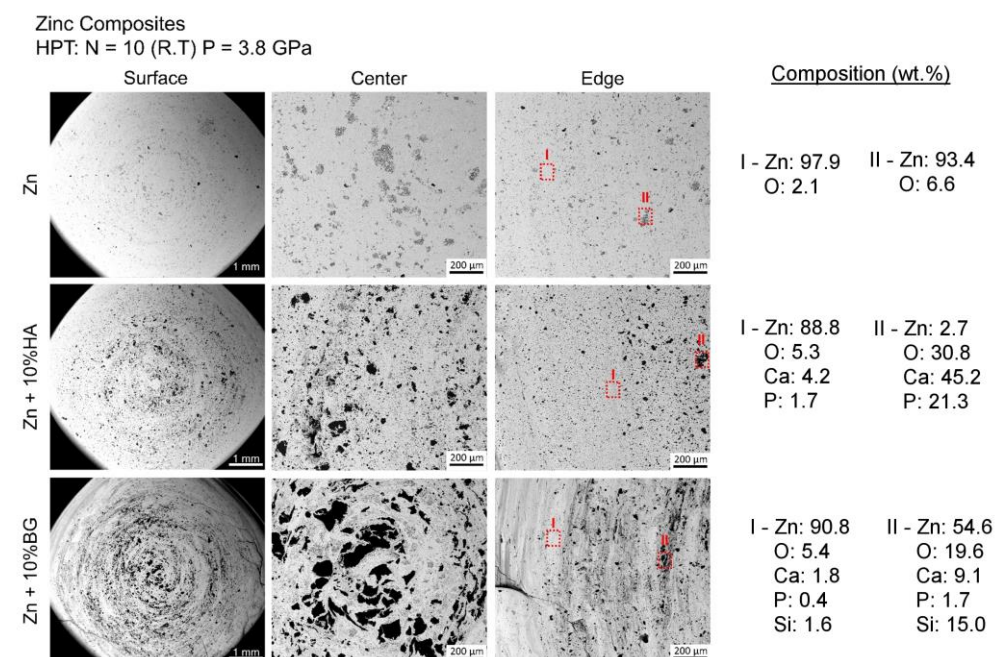

Figure 2. The appearance of the surface of the processed discs.

The average composition of selected locations was evaluated using EDS. The analysis was conducted at two locations for each sample, one representing the matrix area and the other around the reinforcement particles. Thus, the pure Zn sample is composed of Zn, O and islands of higher oxygen content surrounded by a Zn-rich matrix. This is attributed to the zinc oxide layer of the starting powder that becomes part of the composite after consolidation. Small amounts of Ca and P are observed in the matrix of the Zn-HA and Ca, P and Si are present in the matrix of the Zn-BG composites. This shows that small amounts of bioactive glass particles are broken and distributed in the matrix.

Figure 3 shows the average hardness of the composites and it is apparent that the addition of HA and BG increases the strength of the material. The standard deviation of

the measurements shows that the Zn-HA and Zn-BG composites display a larger variation in strength due to the interaction between the reinforcement phase and the surrounding matrix. The size and distribution of the reinforcement phase varies along the disc diameter. The average hardness of the disc of Zn consolidated with HPT is only slightly larger than the value reported for pure Zn processed with HPT of ~38 Hv [14], but the incorporation of hard ceramic particles can increase the hardness to over ~60 Hv. The hardness in the Zn-HA composite processed with HPT is larger than the value reported in the literature for Zn-HA composites processed with spark plasma sintering [21].
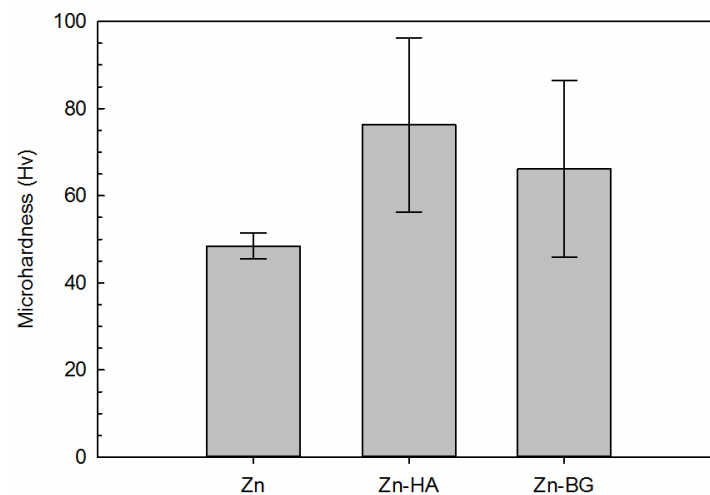

Figure 3. The average microhardness of the composites.

Plane strain compression tests also confirm the higher strength of the Zn-HA and Zn-BG composites. Figure 4 shows the stress vs. strain curves obtained in this test. Thus, the yield stress for the consolidated Zn is ~100 MPa, which agrees with the range of yield stress reported for pure Zn processed with HPT [14]. The flow stress increases to ~160 MPa in the Zn-HA and Zn-BG composites. The Zn-BG composite displays a peak stress of ~180 MPa at a strain of ~0.04, followed by a decrease in flow stress attributed to the propagation of cracks in this material. The consolidated Zn and Zn-HA composite display strain hardening behavior and the flow stress increases with deformation. Flow stress over ~200 MPa is observed in the Zn-HA composite after ~20% strain, which is higher than the peak stress (~150 MPa) observed in pure Zn tested in tension [14]. These results show that the changes in composition and structure due to the incorporation of ceramic particles and HPT processing effectively strengthen the material.

The strain rate sensitivity of the different samples was evaluated using indentation creep tests and following a procedure suggested elsewhere [31]. The indentation depth is plotted as a function of $t-t_c$, where t_c is a constant and t is the indentation time (Figure 5). The strain rate sensitivity was estimated for each material and the values are within the range of 0.032~0.044. This range is slightly lower than the values obtained in tensile tests in commercial purity Zn [37]. It is known that the strain rate sensitivity of zinc depends on the testing strain rate [37], temperature and grain size [3,5,38]. It was recently shown that the strain rate sensitivity of metals depends on multiple thermally activated mechanisms [5]. These mechanisms might include grain size strengthening, solution hardening and second phase particle strengthening. Thus, the present results suggest that the strengthening effect due to hard ceramic particles might decrease the strain rate sensitivity of zinc.
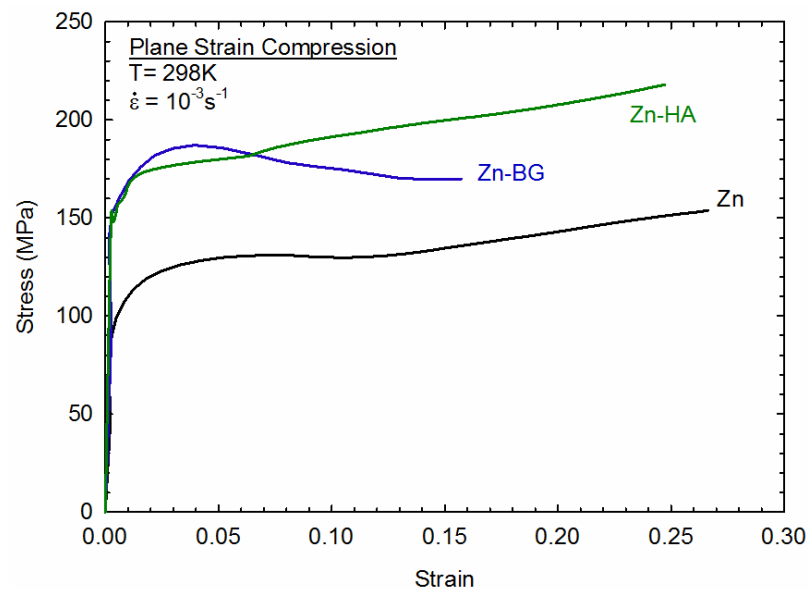
Figure 4. Stress vs. strain curves obtained with plane strain compression testing.
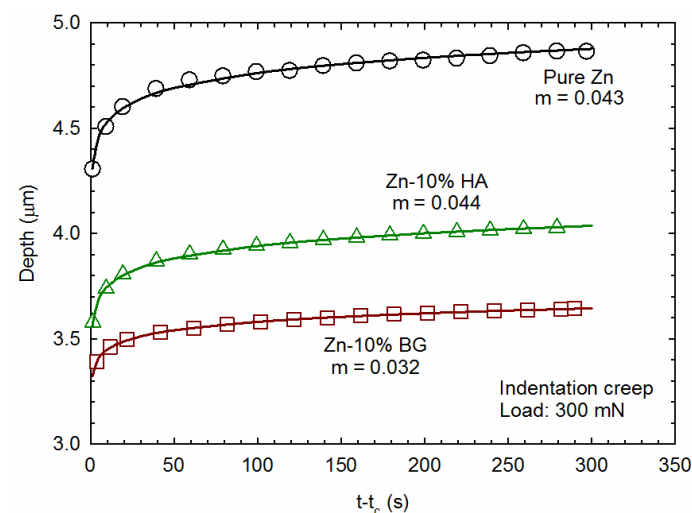

Figure 5. Indentation depth plotted as a function of holding time subtracting the constant t_c.

3.2. Corrosion Behavior

Electrochemical tests were used to evaluate the corrosion behavior of the different materials in the Hank's solution. Figure 6 shows representative potentiodynamic polarization curves. It is observed that the incorporation of HA and BG increases the corrosion potential of the composite compared to consolidated Zn. It also increases the corrosion current and the values determined in experiments are given in Table 1. It is observed that the corrosion current density in consolidated pure Zn agrees with the value of 9.07 $\mu A/cm^2$ reported for rolled pure Zn [39]. Compared to the pure Zn sample, the increase in corrosion current density in the Zn-HA composite also agrees with the trend reported in the literature [21]. The curves of the EIS tests are shown in Figures 7 and 8. The electrochemical impedance spectroscopy (EIS) test shows a decrease in impedance in the Zn-HA composite compared to Zn and an increase in this parameter in the Zn-BG composite. A decrease in impedance was also reported for a Zn-HA composite compared to pure Zn [21]. In Figure 8, it can be observed that the impedance modulus at a frequency of 10^{-2} Hz is higher for the Zn-BG composite. The shape of the frequency versus phase angle curves indicates two-time constants for pure Zn and the Zn-HA composite and a one-time constant for the Zn-BG composite, which suggests different corrosion mechanisms.
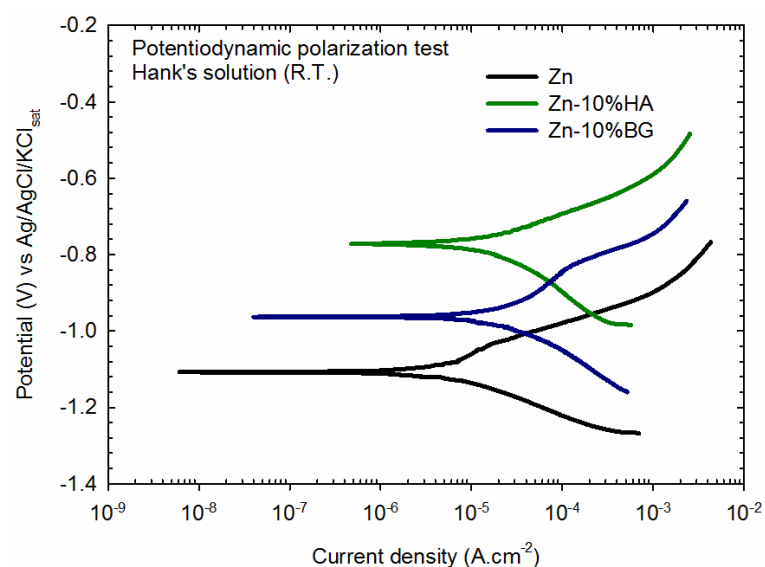
Figure 6. Representative curves obtained in potentiodynamic polarization tests.

Table 1. Summary of average values of corrosion potential (E) and current density (I) determined with potentiodynamic polarization curves.

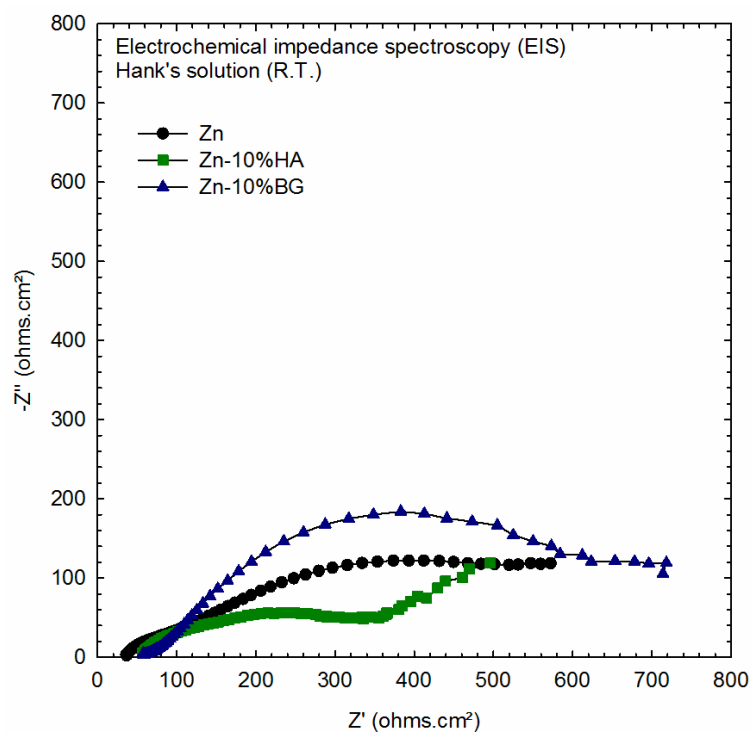| Sample	E (VvsAg/AgCl/KCl$_{sat}$)	I (μA/cm^2)
Zn	-1.12 ± 0.02	6.28 ± 1.59
Zn-HA	-0.80 ± 0.07	16.24 ± 5.10
Zn-BG	-1.00 ± 0.06	20.05 ± 2.62

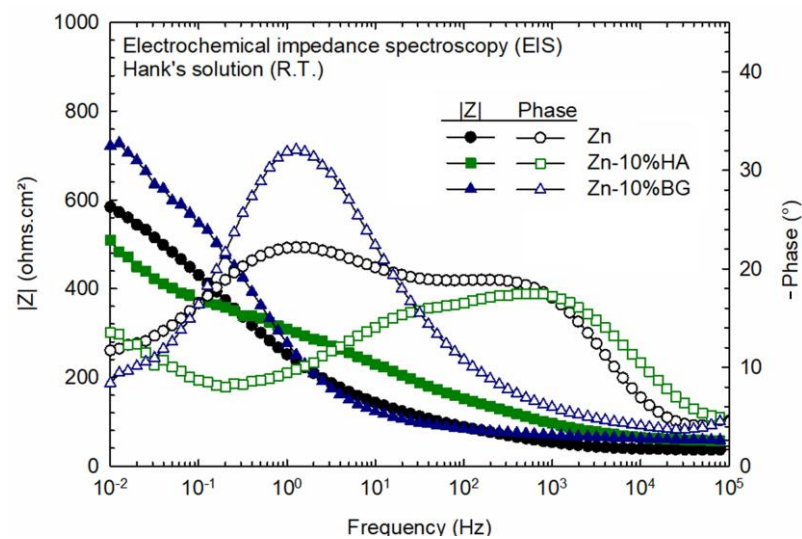**Figure 7.** Nyquist plots obtained for the different samples.

Figure 8. Bode plots for Zn, Zn-10% HA and Zn-10% BG. The filled symbols refer to the |Z| while the empty symbols are related to the phase.

The different samples were subjected to immersion in the Hank's solution for 24 h and their surfaces were observed using SEM. Figure 9 shows the appearance of the different samples. Pure Zn shows no sign of significant corrosion, while a rougher surface develops in the Zn-BG composite, suggesting more corrosion in the latter. The average composition of a large area was evaluated using EDS and the results show the presence of O and minor amounts of Ca and P in the consolidated Zn. The amount of O, Ca and P is larger in the Zn-HA and Zn-BG composites, and could reach higher levels of the Ca/P ratio if it stays in the solution for a longer period, confirming these composites' ability to develop a surface layer rich in these elements. An increase in O, Ca and P concentration was reported for the surface layer of a Zn-10% HA composite compared to a pure Zn counterpart after 50 days of immersion in a Hank's solution [21]. The following was also reported: an increase in the ratio of Ca/P from 0.54 in pure Zn to 1.41 in the Zn-HA composite [21]. This trend agrees with the present results, showing a ratio of 0.51 in pure Zn and 1.05 in the Zn-HA composite.
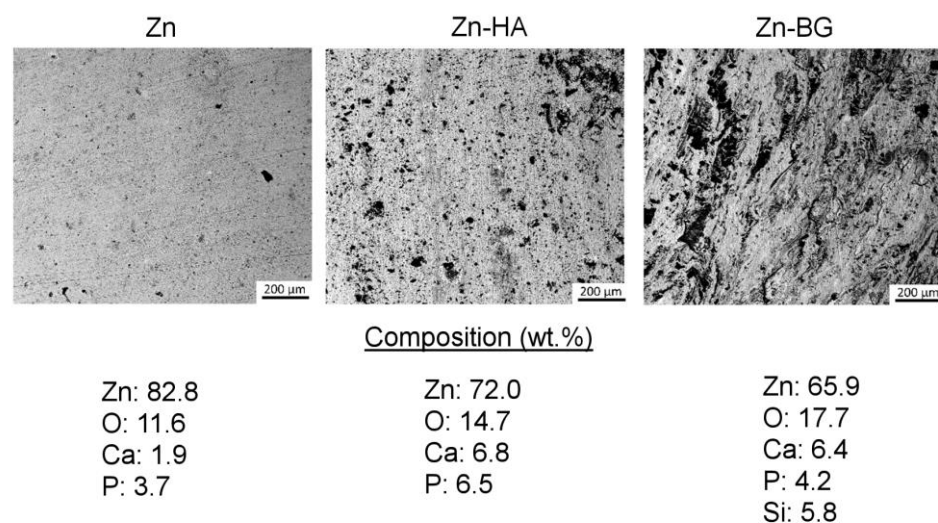

Figure 9. The appearance of the surface of the processed discs and average composition after immersion in Hank's solution for 24 h.

4. Discussion

The present results show it is possible to consolidate Zn particles into a bulk through HPT processing. The large compressive stresses and severe shear straining promotes the elongation of particles, breaking the oxide layer and enabling metal binding. It is also shown that the ZnO particles become dispersed within the matrix during consolidation. Incorporating bioactive particles is also possible and the results show that the breaking and dispersion of these particles increase with increasing straining during HPT. Thus, the particles become smaller and better dispersed at the edges of discs processed using 10 turns of HPT compared to the center of these discs. The effectiveness of the consolidation is verified by the enhanced mechanical strength of the composites. It is expected that the heterogeneity in the disc structure from the center to edge will decrease with increasing the number of turns of HPT [8]. Moreover, eventual differences in the structure are avoided when processing ring samples [40–42] instead of disc-shaped samples. Figure 10 illustrates the procedure and the final structure of the composites. Thus, the initial Zn and bioactive particles are mixed, pressed and consolidated using high-pressure torsion. The final structure can be described as a continuous matrix of Zn containing dispersed ZnO and bioactive particles.
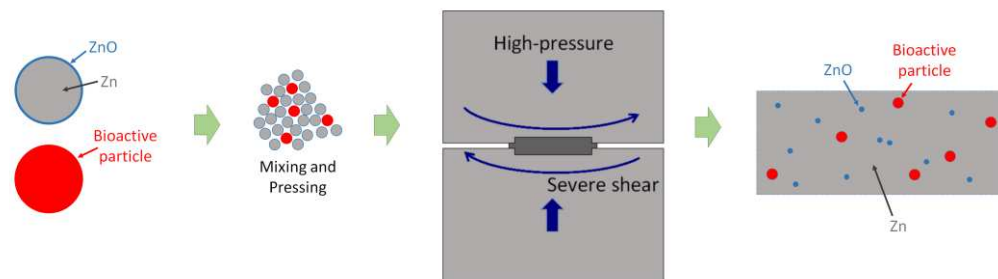

Figure 10. Illustration of the consolidation procedure and final structure of Zn-bioactive particle composites.

The appearance of cracks in the Zn-BG composite is attributed to the expansion of the bioactive glass. Bioactive glass is known for its tendency to induce hydroxyapatite formation [29] and this phenomenon is expected to increase the volume of the original particles.

In order to provide a direct evaluation of the material produced using the consolidation of particles through HPT in the present experiments, the hardness and corrosion rate of Zn produced using different techniques are summarized in Table 2. The data include samples produced using casting, thermo-mechanical processing and consolidation of particles. It is observed that the hardness of the sample produced in the present study is within the upper range of Zn produced using other techniques and the corrosion rate is within the average values.

Table 2. Summary of hardness and corrosion data of Zn processed using different routes.

Processing	Hardness (Hv)	Corr. Rate (mm/Year)	Corr. Test	Corr. Media	Reference
HPT	47.7	0.094	Electrochemical	Hank's	Present study
Casting	41.4	0.019	Immersion	Hank's	[43]
Rolling	42.7	0.011	Immersion	Hank's	[43]
Extrusion-drawing	41.4	0.036	Immersion	Hank's	[44]
Rolling	40.0	0.135	Electrochemical	Hank's	[39]
Casting	30.0	0.137	Immersion	Hank's	[45]
Extrusion	34.0	0.134	Immersion	Hank's	[45]

Table 2. *Cont.*

Processing	Hardness (Hv)	Corr. Rate (mm/Year)	Corr. Test	Corr. Media	Reference
Ball milling + Sintering	18.0	2.710	Electrochemical	Hank's	[46]
Extrusion	34.9	0.410	Immersion	SBF	[47]
Sintering	18.7	0.610	Immersion	SBF	[47]
Sintering	14.4	0.750	Immersion	SBF	[47]
Spark Plasma Sintering	43.9	0.073	Immersion	Hank's	[21]
Spark Plasma Sintering	33.0	0.850	Electrochemical	SBF	[22]
Extrusion	45.6	0.13	Electrochemical	SBF	[23]
Laser Melting System	40.7	0.114	Electrochemical	SBF	[48]
Sintering	58.0	0.264	Electrochemical	Hank's	[49]
Spark Plasma Sintering	47.4	0.105	Electrochemical	SBF	[50]
Sintering	47.3	0.191	Electrochemical	SBF	[19]
Sintering	43.7	0.085	Electrochemical	Hank's	[51]

It is then interesting to compare the data of the Zn-HA and Zn-BG composites produced in the present study with other Zn matrix composites and this is provided in data summarized in Table 3. It is observed that the strength of the composites produced in the present study is in the upper range of pure Zn matrix composites. Higher strength is attained in composites in which Zn alloyed with Mg is used in the matrix [52,53]. The corrosion rates of the Zn-HA and Zn-BG composites are also in the upper range for the different composites. It has been shown that the addition of HA increases the corrosion rate and it was suggested that this effect could be used to adjust the degradation of Zn [21]. Data for Zn-BG composites were not found in the literature, but the present results suggest that bioactive glass leads to a similar effect relative to hydroxyapatite. The chemical and biological stability of HA is higher than the BG, therefore the glass can increase the strength but also the corrosion rate [54].

Structural temporary implants must withstand the load conditions during the period in which the tissue regenerates and should undergo corrosion within a reasonable time afterward. Hence, the corrosion of a temporary implant cannot be faster than the time required for regeneration but also should not be too slow. The length of time for regeneration can vary depending on the tissue and it is important to note that the length of time for corrosion of an implant depends on its corrosion rate and on its dimensions. Thus, the ideal corrosion rate can vary depending on the application and implant dimensions. The ability to control the corrosion rate of Zn by incorporating bioactive particles is therefore desirable and can be used to tailor the lifespan of a temporary implant.

Finally, it has been reported that the addition of hydroxyapatite improves the osteogenic properties of Zn, as observed with in vivo tests [21]. The present study shows a higher concentration of Ca and P on the surface of the Zn-HA composite after 1 day of immersion in the Hank's solution, due to its initial composition, compared to pure Zn. This result suggests that the Zn-HA composite can develop a corrosion product surface layer with a composition closer to the bone, which might improve its performance as a temporary implant for orthopedic applications. The bioactive glass has faster chemical kinetics, which allow for faster and more effective bonding with the bone than HA. A considerable increase in the Ca/P ratio on the material surface is expected due to the formation of carbonated hydroxyapatite when in contact with solutions such as SBF (simulated body fluid) and Hank's [55].

Table 3. Summary of strength and corrosion data of Zn composites.

Composite	Yield Strength (MPa)	Corr. Potential (V)	Corr. Rate (mm/Year)	Corr. Test	Corr. Media	Reference
Zn-10% HA	156	−0.760	0.258	Electrochemical	Hank's	This study
Zn-10% BG	161	−0.960	0.320	Electrochemical	Hank's	This study
Zn-1% Mg	258	−0.946	0.040	Immersion	SBF	[52]
Zn-1% Mg/1β-TCP	277	−0.957	0.045	Immersion	SBF	[52]
Zn-0.5% SiC	43	−1.059	0.148	Electrochemical	SBF	[48]
Zn-1% SiC	75	−1.107	0.163	Electrochemical	SBF	[48]
Zn-2% SiC	122	−1.119	0.198	Electrochemical	SBF	[48]
Zn-3% SiC	44	−1.170	0.230	Electrochemical	SBF	[48]
Zn-0.1% GNP	110	−1.084	0.224	Electrochemical	Hank's	[49]
Zn-0.2% GNP	123	−1.113	0.090	Electrochemical	Hank's	[49]
Zn-0.3% GNP	119	−1.061	0.143	Electrochemical	Hank's	[49]
Zn-0.4% GNP	118	−1.110	0.187	Electrochemical	Hank's	[49]
Zn-3% MgO	156	−0.953	0.171	Electrochemical	SBF	[50]
Zn-3% ZnO	135	−0.960	0.184	Electrochemical	SBF	[50]
Zn-3% CuO	203	−0.963	0.178	Electrochemical	SBF	[50]
Zn-3% Mg-0.7Mg$_2$Si	388	−0.996	0.045	Immersion	Hank's	[53]
Zn-3% Mg-0.7Mg$_2$Si	406	−0.930	0.043	Immersion	Hank's	[53]
Zn–1Mg$_2$Ge	118	−0.714	0.219	Electrochemical	Hank's	[56]
Zn–3Mg$_2$Ge	162	−0.755	0.347	Electrochemical	Hank's	[56]
Zn–5Mg$_2$Ge	129	−0.845	0.026	Electrochemical	Hank's	[56]
Zn/1% TCP	133	-	0.081	Immersion	SBF	[20]
Zn/3% TCP	141	-	0.071	Immersion	SBF	[20]
Zn/5% TCP	123	-	0.081	Immersion	SBF	[20]
Zn/1% TCP	132	−0.915	0.077	Electrochemical	SBF	[19]
Zn/3% TCP	142	−0.928	0.148	Electrochemical	SBF	[19]
Zn/5% TCP	142	−0.927	0.162	Electrochemical	SBF	[19]
Zn-1% Mg	135	−1.066	0.114	Immersion	Hank's	[51]
Zn-2% Mg	152	−1.101	0.209	Immersion	Hank's	[51]
Zn-5% Mg	184	−1.312	0.427	Immersion	Hank's	[51]
Zn-3% HA	108	−1.046	0.101	Electrochemical	SBF	[57]
Zn-3% HA-2% Fe	116	−1.047	0.088	Electrochemical	SBF	[57]
Zn-5% HA-2% Fe	118	−1.071	0.113	Electrochemical	SBF	[57]
Zn-1% HA	70	−1.281	0.327	Immersion	Hank's	[21]
Zn-5% HA	43	−1.274	0.630	Immersion	Hank's	[21]
Zn-10% HA	47	−1.290	0.856	Immersion	Hank's	[21]
Zn-16% HA	46	-	1.520	Electrochemical	SBF	[22]
Zn-8% HA	113	-	0.070	Electrochemical	SBF	[23]

5. Conclusions

Zinc matrix composites were produced with consolidation, at room temperature, of particles using high-pressure torsion (HPT). Zn-10% hydroxyapatite (HA) and Zn-10% bioactive glass (BG) composites were successfully consolidated. A continuous Zn matrix and high strength were observed in all composites.

The reinforcement particles become smaller and their distribution improved with increasing the amount of shear straining during HPT.

The addition of HA and BG to zinc improves the hardness and compressive strength and increases the corrosion rate in a Hank's solution. These adjustments in properties can be used to tailor the size and time required for the corrosion of temporary implants.

A higher amount of Ca and P is observed on the surface of the Zn-HA and Zn-BG composites after immersion in the Hank's solution for 24 h compared to pure Zn.

Data Availability Statement: The data presented in this study are available on request from the corresponding author.

References

1. Zheng, Y.F.; Gu, X.N.; Witte, F. Biodegradable metals. *Mater. Sci. Eng. R Rep.* **2014**, *77*, 1–34. [CrossRef]
2. Edalati, K.; Bachmaier, A.; Beloshenko, V.A.; Beygelzimer, Y.; Blank, V.D.; Botta, W.J.; Bryła, K.; Čížek, J.; Divinski, S.; Enikeev, N.A.; et al. Nanomaterials by severe plastic deformation: Review of historical developments and recent advances. *Mater. Res. Lett.* **2022**, *10*, 163–256. [CrossRef]
3. Figueiredo, R.B.; Langdon, T.G. Effect of grain size on strength and strain rate sensitivity in metals. *J. Mater. Sci.* **2022**, *57*, 5210–5229. [CrossRef]
4. Figueiredo, R.B.; Langdon, T.G. Deformation mechanisms in ultrafine-grained metals with an emphasis on the Hall-Petch relationship and strain rate sensitivity. *J. Mater. Res. Technol.* **2021**, *14*, 137–159. [CrossRef]
5. Figueiredo, R.B.; Kawasaki, M.; Langdon, T.G. Seventy years of Hall-Petch, ninety years of superplasticity and a generalized approach to the effect of grain size on flow stress. *Prog. Mater. Sci.* **2023**, *137*, 101131. [CrossRef]
6. Miyamoto, H.; Yuasa, M.; Rifai, M.; Fujiwara, H. Corrosion Behavior of Severely Deformed Pure and Single-Phase Materials. *Mater. Trans.* **2019**, *60*, 1243–1255. [CrossRef]
7. Miyamoto, H. Corrosion of Ultrafine Grained Materials by Severe Plastic Deformation, an Overview. *Mater. Trans.* **2016**, *57*, 559–572. [CrossRef]
8. Zhilyaev, A.P.; Langdon, T.G. Using high-pressure torsion for metal processing: Fundamentals and applications. *Prog. Mater. Sci.* **2008**, *53*, 893–979. [CrossRef]
9. Figueiredo, R.B.; Langdon, T.G. Processing Magnesium and Its Alloys by High-Pressure Torsion: An Overview. *Adv. Eng. Mater.* **2019**, *21*, 1801039. [CrossRef]
10. Medeiros, M.P.; Lopes, D.R.; Kawasaki, M.; Langdon, T.G.; Figueiredo, R.B. An Overview on the Effect of Severe Plastic Deformation on the Performance of Magnesium for Biomedical Applications. *Materials* **2023**, *16*, 2401. [CrossRef]
11. Hohenwarter, A.; Kammerhofer, C.; Pippan, R. The ductile to brittle transition of ultrafine-grained Armco iron: An experimental study. *J. Mater. Sci.* **2010**, *45*, 4805–4812. [CrossRef]
12. Ivanisenko, Y.; Valiev, R.Z.; Fecht, H.J. Grain boundary statistics in nano-structured iron produced by high pressure torsion. *Mater. Sci. Eng. A* **2005**, *390*, 159–165. [CrossRef]
13. Batista, B.A.; Soares, R.B.; Lins, V.F.C.; Figueiredo, R.B.; Hohenwarter, A.; Matencio, T. Corrosion in Hank's solution and mechanical strength of ultrafine-grained pure iron. *Adv. Eng. Mater.* **2020**, *22*, 2000183. [CrossRef]
14. Srinivasarao, B.; Zhilyaev, A.P.; Langdon, T.G.; Pérez-Prado, M.T. On the relation between the microstructure and the mechanical behavior of pure Zn processed by high pressure torsion. *Mater. Sci. Eng. A* **2013**, *562*, 196–202. [CrossRef]

15. Bednarczyk, W.; Kawałko, J.; Rutkowski, B.; Wątroba, M.; Gao, N.; Starink, M.J.; Bała, P.; Langdon, T.G. Abnormal grain growth in a Zn-0.8Ag alloy after processing by high-pressure torsion. *Acta Mater.* **2021**, *207*, 116667. [CrossRef]

16. Hernández-Escobar, D.; Unocic, R.R.; Kawasaki, M.; Boehlert, C.J. High-pressure torsion processing of Zn–3Mg alloy and its hybrid counterpart: A comparative study. *J. Alloys Compd.* **2020**, *831*, 154891. [CrossRef]

17. Kawasaki, M.; Langdon, T.G. Developing superplasticity and a deformation mechanism map for the Zn–Al eutectoid alloy processed by high-pressure torsion. *Mater. Sci. Eng. A* **2011**, *528*, 6140–6145. [CrossRef]

18. Kawasaki, M.; Ahn, B.; Langdon, T.G. Microstructural evolution in a two-phase alloy processed by high-pressure torsion. *Acta Mater.* **2010**, *58*, 919–930. [CrossRef]

19. Sun, X.; Yu, X.; Li, W.; Chen, M.; Liu, D. Fabrication and characterization of biodegradable zinc matrix composites reinforced by uniformly dispersed beta-tricalcium phosphate via graphene oxide-assisted hetero-agglomeration. *Mater. Sci. Eng. C* **2021**, *130*, 112431. [CrossRef] [PubMed]

20. Zhang, Z.; Liu, D.; Chen, Z.; He, X.; Li, X.; Sun, X. Fabrication, in vitro and in vivo properties of β-TCP/Zn composites. *J. Alloys Compd.* **2022**, *913*, 165223. [CrossRef]

21. Yang, H.; Qu, X.; Lin, W.; Wang, C.; Zhu, D.; Dai, K.; Zheng, Y. In vitro and in vivo studies on zinc-hydroxyapatite composites as novel biodegradable metal matrix composite for orthopedic applications. *Acta Biomater.* **2018**, *71*, 200–214. [CrossRef] [PubMed]

22. Pinc, J.; Čapek, J.; Kubásek, J.; Průša, F.; Hybášek, V.; Veřtát, P.; Sedlářová, I.; Vojtěch, D. Characterization of a Zn-Ca$_5$(PO$_4$)$_3$(OH) Composite with a High Content of the Hydroxyapatite Particles Prepared by the Spark Plasma Sintering Process. *Metals* **2020**, *10*, 372. [CrossRef]

23. Pinc, J.; Čapek, J.; Hybášek, V.; Průša, F.; Hosová, K.; Maňák, J.; Vojtěch, D. Characterization of Newly Developed Zinc Composite with the Content of 8 wt.% of Hydroxyapatite Particles Processed by Extrusion. *Materials* **2020**, *13*, 1716. [CrossRef] [PubMed]

24. Hernández-Escobar, D.; Kawasaki, M.; Boehlert, C.J. Metal hybrids processed by high-pressure torsion: Synthesis, microstructure, mechanical properties and developing trends. *Int. Mater. Rev.* **2022**, *67*, 231–265. [CrossRef]

25. Hernández-Escobar, D.; Marcus, J.; Han, J.-K.; Unocic, R.R.; Kawasaki, M.; Boehlert, C.J. Effect of post-deformation annealing on the microstructure and micro-mechanical behavior of Zn–Mg hybrids processed by High-Pressure Torsion. *Mater. Sci. Eng. A* **2020**, *771*, 138578. [CrossRef]

26. Hernández-Escobar, D.; Rahman, Z.U.; Yilmazer, H.; Kawasaki, M.; Boehlert, C.J. Microstructural evolution and intermetallic formation in Zn-Mg hybrids processed by High-Pressure Torsion. *Philos. Mag.* **2019**, *99*, 557–584. [CrossRef]

27. Castro, M.M.; Montoro, L.A.; Isaac, A.; Kawasaki, M.; Figueiredo, R.B. Mechanical mixing of Mg and Zn using high-pressure torsion. *J. Alloys Compd.* **2021**, *869*, 159302. [CrossRef]

28. Hench, L.L. Bioceramics. *J. Am. Ceram. Soc.* **1998**, *81*, 1705–1728. [CrossRef]

29. dos Santos, D.M.M.; de Carvalho, S.M.; Pereira, M.M.; Houmard, M.; Nunes, E.H.M. Freeze-cast composite scaffolds prepared from sol-gel derived 58S bioactive glass and polycaprolactone. *Ceram. Int.* **2019**, *45*, 9891–9900. [CrossRef]

30. Pereira, P.H.R.; Figueiredo, R.B.; Huang, Y.; Cetlin, P.R.; Langdon, T.G. Modeling the temperature rise in high-pressure torsion. *Mater. Sci. Eng. A* **2014**, *593*, 185–188. [CrossRef]

31. Chinh, N.Q.; Szommer, P. Mathematical description of indentation creep and its application for the determination of strain rate sensitivity. *Mater. Sci. Eng. A* **2014**, *611*, 333–336. [CrossRef]

32. Carvalho, A.P.; Reis, L.M.; Pinheiro, R.P.R.P.; Pereira, P.H.R.; Langdon, T.G.; Figueiredo, R.B. Using Plane Strain Compression Test to Evaluate the Mechanical Behavior of Magnesium Processed by HPT. *Metals* **2022**, *12*, 125. [CrossRef]

33. Su, Y.; Wang, K.; Gao, J.; Yang, Y.; Qin, Y.-X.; Zheng, Y.; Zhu, D. Enhanced cytocompatibility and antibacterial property of zinc phosphate coating on biodegradable zinc materials. *Acta Biomater.* **2019**, *98*, 174–185. [CrossRef]

34. Mollaei, N.; Razavi, S.; Aboutalebi, M.; Fatemi, S. Effect of Mn addition on the microstructure, mechanical, and corrosion properties of an extruded biodegradable Zn-0.2 Mg alloy. *J. Mater. Res. Technol.* **2023**, *22*, 1983–1998. [CrossRef]

35. Hing, K.; Best, S.; Bonfield, W. Characterization of porous hydroxyapatite. *J. Mater. Sci. Mater. Med.* **1999**, *10*, 135–145. [CrossRef]

36. Chen, Q.Z.; Thompson, I.D.; Boccaccini, A.R. 45S5 Bioglass®-derived glass–ceramic scaffolds for bone tissue engineering. *Biomaterials* **2006**, *27*, 2414–2425. [CrossRef]

37. Wagoner, R.H. Strain-rate sensitivity of zinc sheet. *Metall. Mater. Trans. A* **1984**, *15*, 1265–1271. [CrossRef]

38. Lee, J.D.; Niessen, P. Superplasticity in a new dispersion strengthened zinc alloy. *Metall. Trans.* **1973**, *4*, 949–957. [CrossRef]

39. Li, H.; Xie, X.; Zheng, Y.F.; Cong, Y.; Zhou, F.; Qiu, K.; Wang, X.; Chen, S.; Huang, L.; Tian, L. Development of biodegradable Zn-1X binary alloys with nutrient alloying elements Mg, Ca and Sr. *Sci. Rep.* **2015**, *5*, 10719. [CrossRef] [PubMed]

40. Harai, Y.; Edalati, K.; Horita, Z.; Langdon, T.G. Using ring samples to evaluate the processing characteristics in high-pressure torsion. *Acta Mater.* **2009**, *57*, 1147–1153. [CrossRef]

41. Edalati, K.; Horita, Z. Scaling-Up of High Pressure Torsion Using Ring Shape. *Mater. Trans.* **2009**, *50*, 92–95. [CrossRef]

42. Harai, Y.; Ito, Y.; Horita, Z. High-pressure torsion using ring specimens. *Scr. Mater.* **2008**, *58*, 469–472. [CrossRef]

43. Huang, T.; Liu, Z.; Wu, D.; Yu, H. Microstructure, mechanical properties, and biodegradation response of the grain-refined Zn alloys for potential medical materials. *J. Mater. Res. Technol.* **2021**, *15*, 226–240. [CrossRef]

44. Liu, X.; Sun, J.; Yang, Y.; Pu, Z.; Zheng, Y. In vitro investigation of ultra-pure Zn and its mini-tube as potential bioabsorbable stent material. *Mater. Lett.* **2015**, *161*, 53–56. [CrossRef]

45. Mostaed, E.; Sikora-Jasinska, M.; Mostaed, A.; Loffredo, S.; Demir, A.; Previtali, B.; Mantovani, D.; Beanland, R.; Vedani, M. Novel Zn-based alloys for biodegradable stent applications: Design, development and in vitro degradation. *J. Mech. Behav. Biomed. Mater.* **2016**, *60*, 581–602. [CrossRef] [PubMed]

46. Bagha, P.S.; Khaleghpanah, S.; Sheibani, S.; Khakbiz, M.; Zakeri, A. Characterization of nanostructured biodegradable Zn-Mn alloy synthesized by mechanical alloying. *J. Alloys Compd.* **2018**, *735*, 1319–1327. [CrossRef]

47. Čapek, J.; Jablonská, E.; Lipov, J.; Kubatík, T.F.; Vojtěch, D. Preparation and characterization of porous zinc prepared by spark plasma sintering as a material for biodegradable scaffolds. *Mater. Chem. Phys.* **2018**, *203*, 249–258. [CrossRef]

48. Gao, C.; Yao, M.; Shuai, C.; Peng, S.; Deng, Y. Nano-SiC reinforced Zn biocomposites prepared via laser melting: Microstructure, mechanical properties and biodegradability. *J. Mater. Sci. Technol.* **2019**, *35*, 2608–2617. [CrossRef]

49. Kabir, H.; Munir, K.; Wen, C.; Li, Y. Microstructures, mechanical and corrosion properties of graphene nanoplatelet–reinforced zinc matrix composites for implant applications. *Acta Biomater.* **2023**, *157*, 701–719. [CrossRef]

50. Sun, X.; Yu, X.; Li, W.; Chen, M.; Liu, D. Mechanical properties, degradation behavior and cytocompatibility of biodegradable 3vol% X (X = MgO, ZnO and CuO)/Zn matrix composites with excellent dispersion property fabricated by graphene oxide-assisted hetero-aggregation. *Biomater. Adv.* **2022**, *134*, 112722. [CrossRef]

51. Yang, H.; Qu, X.; Lin, W.; Chen, D.; Zhu, D.; Dai, K.; Zheng, Y. Enhanced osseointegration of Zn-Mg composites by tuning the release of Zn ions with sacrificial Mg-rich anode design. *ACS Biomater. Sci. Eng.* **2018**, *5*, 453–467. [CrossRef]

52. Xu, Y.; Zhang, Z.; Liu, D.; Zhao, Y.; Sun, X. Microstructure and properties of β-TCP/Zn-1Mg composites processed by hot extrusion combination of multi-pass ECAP. *J. Alloys Compd.* **2022**, *903*, 163988. [CrossRef]

53. Tong, X.; Cai, W.; Lin, J.; Wang, K.; Jin, L.; Shi, Z.; Zhang, D.; Lin, J.; Li, Y.; Dargusch, M. Biodegradable Zn− 3Mg− 0.7 Mg2Si composite fabricated by high-pressure solidification for bone implant applications. *Acta Biomater.* **2021**, *123*, 407–417. [CrossRef] [PubMed]

54. Ghaebi Panah, N.; Atkin, R.; Sercombe, T.B. Bioactivity and biodegradability of high temperature sintered 58S ceramics. *J. Eur. Ceram. Soc.* **2022**, *42*, 3614–3623. [CrossRef]

55. Du, R.L.; Chang, J.; Ni, S.Y.; Zhai, W.Y.; Wang, J.Y. Characterization and in vitro bioactivity of zinc-containing bioactive glass and glass-ceramics. *J. Biomater. Appl.* **2006**, *20*, 341–360. [CrossRef]

56. Tong, X.; Wang, H.; Zhu, L.; Han, Y.; Wang, K.; Li, Y.; Ma, J.; Lin, J.; Wen, C.; Huang, S. A biodegradable in situ Zn–Mg2Ge composite for bone-implant applications. *Acta Biomater.* **2022**, *146*, 478–494. [CrossRef] [PubMed]

57. Pathak, D.K.; Pandey, P.M. Evaluation of in vitro corrosion behavior of zinc–hydroxyapatite and zinc–hydroxyapatite–iron as biodegradable composites. *J. Biomed. Mater. Res. Part B Appl. Biomater.* **2021**, *109*, 436–450. [CrossRef] [PubMed]